International Journal of Thermal Sciences 48 (2009) 2046–2052

Contents lists available at ScienceDirect

International Journal of Thermal Sciences

journal homepage: www.elsevier.com/locate/ijts

Transient behavior of vascularized walls exposed to sudden heating

S. Kim [a], S. Lorente [b], A. Bejan [a,*]

[a] Department of Mechanical Engineering and Materials Science, Duke University, Durham, NC 27708-0300, USA
[b] Laboratoire Matériaux et Durabilité des Constructions, Département de Génie Civil, Université de Toulouse, INSA, 135 Avenue de Rangueil, 31077 Toulouse, France

ARTICLE INFO

Article history:
Received 17 October 2008
Received in revised form
7 January 2009
Accepted 31 March 2009
Available online 8 May 2009

Keywords:
Constructal
Vascularized
Turbine blade cooling
Dendritic
Volumetric cooling
Svelteness
Smart materials
Self-cooling
Optimal spacings
Designed porous media

ABSTRACT

Vascular flow architectures are proposed for controlling the temperature of walls that are subjected suddenly to intense heating from one side. After a short delay, single-phase coolant starts flowing from the other side, and fights off the heating effect. The time-dependent behavior of such vascularized composites is studied and optimized based on full numerical simulations of transient conjugate heat transfer. The focus is on the hot-spot temperatures that build up inside the composite – their evolution, spatial migration, and highest levels. Of interest are vasculature designs that keep the hot-spot temperatures below the safe level associated with long-term operation with steady heating from one side and steady coolant flow from the other side. It is shown that when the driving pressure difference is fixed, the approach to the steady-state temperature is the shortest when the dendrites have an optimal (finite) number of bifurcation levels. The allowable delay time is approximately the same as the duration that the hot-spot temperature reaches the steady-state hot-spot temperature in the absence of coolant.

1. Vascular designs

Constructal theory [1–3] is the view that the generation of flow configuration is a physics phenomenon, and summarizes it as a principle of physics (the constructal law): "for a flow system to persist in time (to live) it must evolve in such a way that it provides easier and easier access to the currents that flow through it" [2].

The current literature shows that the constructal law is used as a scientific principle in engineering design. This body of work was reviewed most recently in Refs. [1,4,5]. Special among the engineering flow architectures derived from the constructal theory are the dendritic (tree-shaped) designs. They are a promising replacement for the traditional engineering flow configurations such as arrays of parallel channels, because tree-shaped configurations are the most effective connections from a point to volume and from volume to a point. This advantage is why tree-shaped designs are now appearing in active technological domains such as manufacturing [6], electronics cooling [7], fuel cells [8], and compact heat exchanger [9–15].

The constructal design work that has been done so far is mainly for steady-state thermal/flow systems. The transient behavior however is critical in applications where sudden, time-dependent heating is the norm (electronics, avionics, thermal management of aircraft, etc.). In this paper we consider this fundamental phenomenon as a time-dependent problem of conjugate heat transfer in a vascularized wall with intense heating from the side and coolant flowing from the other side.

The tree-shaped flow (Fig. 1) endows the wall with the flow architecture that has a global flow resistance close to the lowest level possible [16,17]. At the time $t = 0$, the heat flux q'' impinges on the left side of the wall. After a short delay ($t = t_d$), the coolant flows from right to left, and is driven by the pressure difference imposed across the wall. Here we investigate the transient thermal performance of the vascular wall, by focusing on the evolution of the peak (hot-spot) temperatures inside the wall material.

2. Numerical formulation

We modeled numerically the transient response of a solid wall of thickness L that is heated with uniform heat flux q'' from the left side (Fig. 1). The right side is insulated. The wall is cooled by a single-phase fluid driven by a specified pressure difference ΔP. The wall has many elemental volumes of the kind shown in Fig. 1.

* Corresponding author. Tel.: +1 919 660 5314; fax: +1 919 660 8963.
E-mail address: abejan@duke.edu (A. Bejan).

1290-0729/$ – see front matter © 2009 Elsevier Masson SAS. All rights reserved.
doi:10.1016/j.ijthermalsci.2009.03.019

Nomenclature

Be	dimensionless pressure difference, Bejan number, Eq. (25)
c_p	specific heat at constant pressure, J/kg K
d	smallest length scale, m
D_i	channel diameters, m
H	height, m, Fig. 1
k	thermal conductivity, W/m K
$\tilde{k}$	ratio of thermal conductivities, Eq. (24)
L	length, m
$\dot{m}$	mass flow rate, kg/s, Fig. 1
p	number of pairing levels
P	pressure, Pa
Pr	Prandtl number, Eq. (24)
q''	heat flux, W/m^2
Sv	svelteness number, Eq. (2)
t	time, s
t_c	thermal inertia time, s
t_{ss}	characteristic response time, s, Eq. (26)
T	temperature, K
$\tilde{T}$	dimensionless excess temperature, Eq. (13)
u, v, w	velocity components, m/s
V_c	total volume of channels, m^3
x, y, z	Cartesian coordinates, m

Greek letters

α	thermal diffusivity, m^2/s
ΔP	pressure drop, Pa
μ	viscosity, kg/s m
ν	kinematic viscosity, m^2/s
ρ	density, kg/m^3
ϕ	porosity, void fraction
τ	time delay fraction, Eq. (28)

Subscripts

d	delay
f	fluid
max	maximum, hot spot
min	minimum
out	outlet
s	solid
ss	steady state

All the channels are round, and the diameters of the channels are sized relative to one another in accordance with the Hess–Murray law [1,18,19],

$$\frac{D_i}{D_{i+1}} = 2^{1/3} \quad (i = 1, 2, \ldots, p) \tag{1}$$

The thickness of the element in the direction perpendicular to the figure is set equal to the spacing d. The vertical dimension H of one element is $2^{p+1}d$, where p is the number of pairing levels (e.g. $p = 3$ in Fig. 1). Several volume elements stacked in the vertical direction in Fig. 1 constitute a slab vascularized with line-to-line tree structures. In the present study we conducted simulations for structures with $p = 1$, 2, 3 and 4.

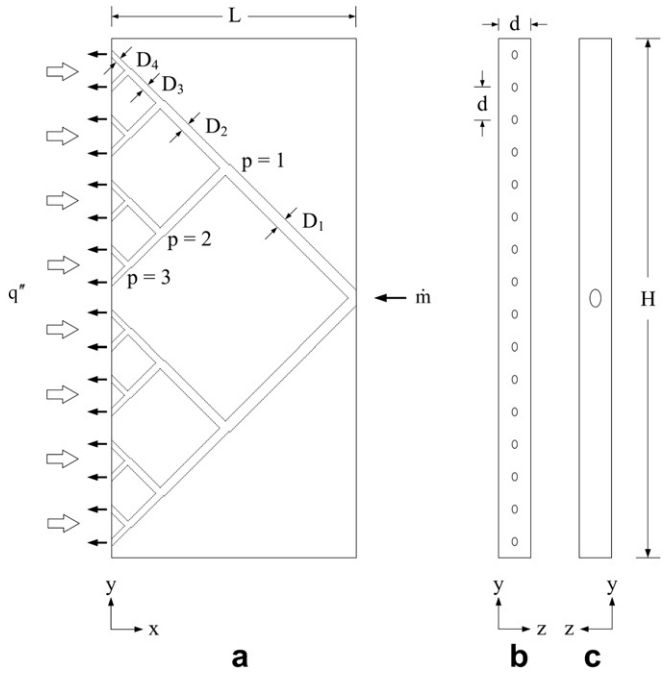

Fig. 1. Tree-shaped flow structure with three levels of bifurcation: (a) the mid plane of the flow element; (b) the view from the left, showing the outlets; and (c) the view from the right, showing the inlet.

The porosity was fixed at $\phi = 0.05$. By "porosity" we mean the volume fraction occupied by all the channels. The vascular structure is not a porous medium in the usual sense, yet, its volume fraction is fixed, for two reasons. Most applications of vascular designs for self-cooling are projected for future vehicles (e.g. aircraft). In such applications, the mass of the structure (mostly solid mass) is fixed, and so is its volume (solid and fluid). These mass and volume constraints translate into a fixed ϕ value, which is the choice made in the present work.

Eq. (1) was selected as a design rule because of its simplicity, and because it is a robust approximation [1] of the optimal ratio of diameters when the flow conditions deviate from the Hess–Murray scenario (Poiseuille flow, one stream divided equally into two streams). In this paper, junction losses and bifurcation asymmetry are taken into account, and consequently the ratio of the flow rates after bifurcation varies in the range 1.3–1.8. The more general form of the Hess–Murray bifurcation rule is given on p. 166 of Ref. [1]. In this paper the bifurcations are asymmetric to the point that each looks more like the letter λ, not Y.

The configuration of a single tree is based on the minimal-lengths method proposed in Ref. [17]. The bifurcations with 90° angles perform very close to the best bifurcations [16]. For example, the global flow resistance of a minimal-length Y-shaped structure exceeds by only 0.5% the global resistance of a fully optimized Y construct [16].

Tree configurations for convection have been studied several authors [3,7–13] by assuming fully developed laminar flow in all the channels. More recently, it was shown that the effect of junction losses is not negligible when the svelteness number *Sv* is less than 10,

$$Sv = \frac{\text{external flow length scale}}{\text{internal flow length scale}} = \frac{L}{V_c^{1/3}} \tag{2}$$

Svelteness is a global geometric property of the flow architecture [20]: it represents the "thinness" of all the lines of the drawing. In the $Sv < 10$ domain the channels are relatively thick, and full numerical simulations of the flow near every junction and corner are necessary.

Another flow feature that becomes accentuated when $Sv < 10$ is the nonuniformity of the flow rates through channels of the same rank. The flow splitting nonuniformity is due to the asymmetry of each Y-shaped construct. Because of inertia, more fluid flows along the straight channel downstream from every bifurcation.

In the present study we used full numerical simulations because the total flow volume V_c and corresponding porosity ($\phi = 0.05$) were such that Sv varied from 2.8 for $p = 1$, to 6.7 for $p = 4$. The flow and temperature fields were simulated as a time-dependent conjugate heat transfer phenomenon by using a finite volume CFD code [21]. The conservation equations for mass and momentum in the flow volume are

$$\frac{\partial u}{\partial x} + \frac{\partial v}{\partial y} + \frac{\partial w}{\partial z} = 0 \tag{3}$$

$$\rho\left(\frac{\partial u}{\partial t} + u\frac{\partial u}{\partial x} + v\frac{\partial u}{\partial y} + w\frac{\partial u}{\partial z}\right) = -\frac{\partial P}{\partial x} + \mu\nabla^2 u \tag{4}$$

$$\rho\left(\frac{\partial v}{\partial t} + u\frac{\partial v}{\partial x} + v\frac{\partial v}{\partial y} + w\frac{\partial v}{\partial z}\right) = -\frac{\partial P}{\partial y} + \mu\nabla^2 v \tag{5}$$

$$\rho\left(\frac{\partial w}{\partial t} + u\frac{\partial w}{\partial x} + v\frac{\partial w}{\partial y} + w\frac{\partial w}{\partial z}\right) = -\frac{\partial P}{\partial z} + \mu\nabla^2 w \tag{6}$$

where $\nabla^2 = \partial^2/\partial x^2 + \partial^2/\partial y^2 + \partial^2/\partial z^2$, where x, y, and z are defined in Fig. 1. The conservation of energy in the fluid and solid volumes is governed by

$$(\rho c_p)_f\left(\frac{\partial T}{\partial t} + u\frac{\partial T}{\partial x} + v\frac{\partial T}{\partial y} + w\frac{\partial T}{\partial z}\right) = k_f\nabla^2 T \tag{7}$$

$$(\rho c_p)_s\frac{\partial T}{\partial t} = k_s\nabla^2 T \tag{8}$$

Heat flux is imposed from the left side in Fig. 1,

$$q'' = -k_s\frac{\partial T}{\partial x} \tag{9}$$

The continuity of heat flux across the solid–fluid interfaces is expressed by

$$k_s\frac{\partial T}{\partial n} = k_f\frac{\partial T}{\partial n} \tag{10}$$

where n is the direction normal to the surface, and k_s and k_f are the thermal conductivities of the solid and the fluid. For greater generality, we determined the flow and temperature fields in terms of the dimensionless variables

$$(\tilde{x}, \tilde{y}, \tilde{z}, \tilde{n}) = (x, y, z, n)/L \tag{11}$$

$$(\tilde{u}, \tilde{v}, \tilde{w}) = (u, v, w)L/\alpha_f \tag{12}$$

$$\tilde{t} = \alpha_f t/L^2 \tag{13}$$

$$\tilde{P} = (P - P_{out})L^2/(\mu\alpha_f) \tag{14}$$

$$\tilde{T} = (T - T_{min})k_s/(q''L) \tag{15}$$

where P_{out} is the lowest pressure (at the outlets), and T_{min} is lowest temperature (at the coolant inlets). Written in terms of dimensionless variables, Eqs. (3)–(10) become

$$\frac{\partial \tilde{u}}{\partial \tilde{x}} + \frac{\partial \tilde{v}}{\partial \tilde{y}} + \frac{\partial \tilde{w}}{\partial \tilde{z}} = 0 \tag{16}$$

$$\frac{1}{Pr}\left(\frac{\partial \tilde{u}}{\partial \tilde{t}} + \tilde{u}\frac{\partial \tilde{u}}{\partial \tilde{x}} + \tilde{v}\frac{\partial \tilde{u}}{\partial \tilde{y}} + \tilde{w}\frac{\partial \tilde{u}}{\partial \tilde{z}}\right) = -\frac{\partial \tilde{P}}{\partial \tilde{x}} + \nabla^2\tilde{u} \tag{17}$$

$$\frac{1}{Pr}\left(\frac{\partial \tilde{v}}{\partial \tilde{t}} + \tilde{u}\frac{\partial \tilde{v}}{\partial \tilde{x}} + \tilde{v}\frac{\partial \tilde{v}}{\partial \tilde{y}} + \tilde{w}\frac{\partial \tilde{v}}{\partial \tilde{z}}\right) = -\frac{\partial \tilde{P}}{\partial \tilde{y}} + \nabla^2\tilde{v} \tag{18}$$

$$\frac{1}{Pr}\left(\frac{\partial \tilde{w}}{\partial \tilde{t}} + \tilde{u}\frac{\partial \tilde{w}}{\partial \tilde{x}} + \tilde{v}\frac{\partial \tilde{w}}{\partial \tilde{y}} + \tilde{w}\frac{\partial \tilde{w}}{\partial \tilde{z}}\right) = -\frac{\partial \tilde{P}}{\partial \tilde{z}} + \nabla^2\tilde{w} \tag{19}$$

$$\frac{\partial \tilde{T}}{\partial \tilde{t}} + \tilde{u}\frac{\partial \tilde{T}}{\partial \tilde{x}} + \tilde{v}\frac{\partial \tilde{T}}{\partial \tilde{y}} + \tilde{w}\frac{\partial \tilde{T}}{\partial \tilde{z}} = \nabla^2\tilde{T} \tag{20}$$

$$\frac{\partial \tilde{T}}{\partial \tilde{t}} = \tilde{\alpha}\nabla^2\tilde{T} \tag{21}$$

$$1 = -\frac{\partial \tilde{T}}{\partial \tilde{x}} \tag{22}$$

$$\tilde{k}\left.\frac{\partial \tilde{T}}{\partial \tilde{n}}\right|_s = \left.\frac{\partial \tilde{T}}{\partial \tilde{n}}\right|_f \tag{23}$$

where the dimensionless groups are

$$Pr = \frac{\nu}{\alpha_f} \quad \tilde{k} = \frac{k_s}{k_f} \quad \tilde{\alpha} = \frac{\alpha_s}{\alpha_f} \tag{24}$$

The imposed pressure difference ΔP is accounted for by the dimensionless difference named Bejan number [22,23],

$$Be = \frac{\Delta P L^2}{\alpha_f \mu} \tag{25}$$

In this paper, the range covered by Be is 10^6–10^{10}, which corresponds to Reynolds numbers (based on water, and channel diameter) less than 500. The flow is laminar, with junction losses taken into account, and with negligible volumetric heating due to viscous dissipation.

The dimensionless conjugate heat transfer problem was solved with the segregated solid energy solver and segregated fluid flow and temperature solvers that the CFD code [21] provides. The convection terms were discretized using the second order upwind scheme, with the secondary gradient option enabled. An algebraic multigrid algorithm was used to solve the linear matrices. The grid fineness was determined by increasing the number of elements in steps of 1000. The number of elements is selected based on the criterion $\varepsilon = (T_i - T_{i-1})/T_{i-1} \le 0.005$, where T_i is the hot-spot temperature computed for the ith step.

The time-dependent evolution of the flow and temperature fields has two distinct time intervals. In the first, the coolant is assumed to flow steadily due to the imposed pressure difference Be, before heating is imposed from the side. The purpose of the simulation of this first interval is to find the thermal response of the vascularized wall, and to compare it with the thermal response of a solid wall without channels ($\phi = 0$).

The second time interval follows after heating is imposed. In practical applications a sensor detects the heating, after which an actuator pumps the coolant. There is an unavoidable time delay between sensing and actuating. In the following simulations the

vascularized flow architecture has a specified time delay (t_d). The objective is to determine the longest allowable delay such that the vascular body does not overheat.

The results are presented in dimensionless form. In an order of magnitude sense, if the wall is stainless steel and the coolant is water, and if $L = 1$ cm, then the results correspond to steady-state conditions with 135 K excess temperature at the hot spots with $q'' = 10^6$ W/m^2, $Be = 10^8$ and $p = 3$. Under the same conditions, in the transient state (Fig. 7 later in this paper) the time constant t_c is 1.08 s, and the hot-spot temperature overshoots the steady-state peak temperature by 22 K.

3. Constant coolant flow rate

The initial conditions are (1) the temperature is uniform over the entire system, at the lowest level (coolant inlet temperature, T_{min}), and (2) the fluid flow is steady and driven by the pressure difference Be. At the time $t = 0^+$, the left side of the wall is exposed to the heat flux q''.

Throughout this work we monitored the highest temperature ($\tilde{T}_{max}$), not the locations where the hot spots occur. It is important to note that the locations change as the parameters change (Be, p), and as time increases. To this aspect we return in the next section. Fig. 2 shows the evolution of the hot-spot temperature when the pressure difference is fixed at $Be = 10^8$. Each curve represents a flow structure (Fig. 1) defined by the number of pairing levels, p. In the large-$\tilde{t}$ limit, the peak temperature $\tilde{T}_{max}$ reaches a steady-state level that depends on p and Be. We define a dimensionless time to characterize the time evolution of the dimensionless peak temperature. The characteristic response time $\tilde{t}_{ss}$ is the time when the hot-spot temperature $\tilde{T}_{max}$ reaches 90% of the steady-state level of the hot-spot temperature $\tilde{T}_{max,ss}$,

$$\tilde{T}_{max}\left(\tilde{t}_{ss}\right) = 0.9\tilde{T}_{max,ss} \tag{26}$$

The 0.9 value is a choice that we made. A more traditional choice for "time-constant" estimates would be 0.637. Another choice, from the Blasius formula for the laminar boundary layer thickness would be 0.99. All these choices work in the same way. Once a convention is made (e.g. 0.9 is fixed), all the results and conclusions are the same in relative terms.

Fig. 3 is a summary of how the steady-state peak temperatures $\tilde{T}_{max,ss}$ depend on Be and the complexity of the architecture (p) when the total flow volume is fixed. The cooling performance improves (i.e. $\tilde{T}_{max,ss}$ decreases) as the applied pressure difference

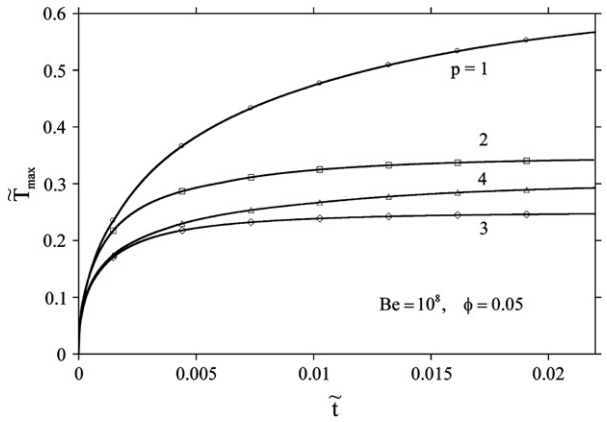

Fig. 2. The evolution of the dimensionless peak temperature in structures with $p = 1$, 2, 3 and 4 ($Be = 10^8$, $\phi = 0.05$).

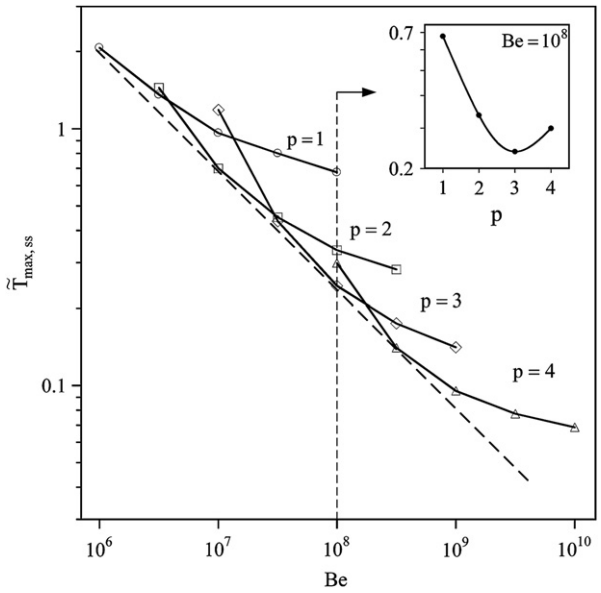

Fig. 3. Steady-state peak temperatures versus the pressure difference and number of bifurcation levels.

(Be) increases, however, the rate of this improvement decreases. Diminishing returns suggest that the way to lower $\tilde{T}_{max,ss}$ values is by changing the entire architecture, from p to $p + 1$. For example, it is better to cool with the $p = 3$ structure than with the $p = 2$ when Be exceeds approximately 3×10^7, and even better with the $p = 4$ structure when Be exceeds 2×10^8.

Another noteworthy feature of Fig. 3 is that the best flow architecture is not the most complex. Every finite Be range has its own best configuration (p), which is small or moderate, not very large. For example, when $Be = 10^8$ the recommended vasculature has $p = 3$. For a larger Be, the recommended p will be larger than 3, but still moderate, not very large. Consequently, an effective cooling regime is obtained not only with a high pressure difference but also with an optimized number of bifurcation levels.

A less complex configuration has a higher flow rate at outlets, but it also has a larger distance between outlets (d). For suppressing hot spots, more flow is beneficial while a larger d is not. The optimal complexity for a certain Be value comes from balancing these competing effects.

The transient behavior en route to steady state also depends on Be and p. Fig. 4 shows the characteristic response time $\tilde{t}_{ss}$, which, when Be is specified, is minimum for a certain configuration (p). The characteristic time is plotted versus Be in Fig. 5, and its behavior is similar to that of the steady-state peak temperature.

4. Time delay

The main objective of the vascularized wall design is to protect the wall from overheating. In practice a time delay ($\tilde{t}_d$) exists between sensing and actuating, that is before the pumping of the coolant begins. If the delay is too long, the peak temperatures will exceed the steady-state level. The key design question is how long a response delay is permissible.

The allowable time delay is determined by two factors. One is how fast the vascularized wall is cooled by the coolant, and this is associated with the characteristic response time that we have studied in the previous section. The other accounts for how fast the peak temperature rises during the delay, when there is no coolant. If the peak temperature increases slowly during the delay, and

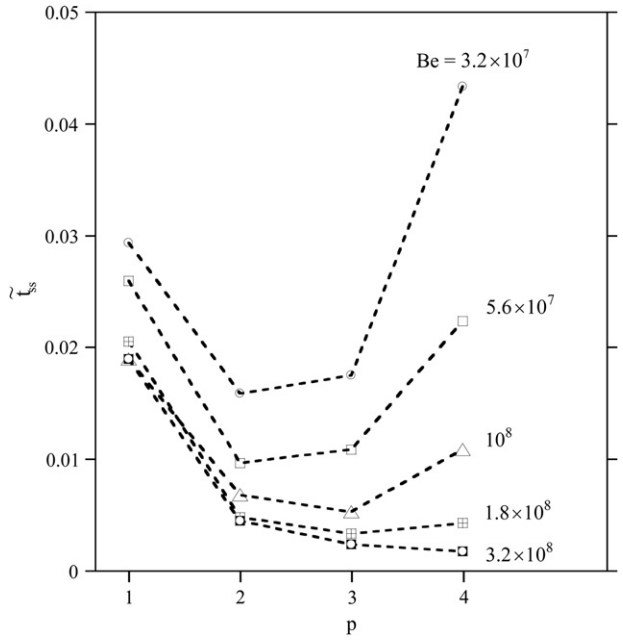

Fig. 4. The characteristic response time $\tilde{t}_{ss}$ versus the number of bifurcation levels.

responds fast after the coolant starts flowing, then the allowable time delay is long, which is an attractive feature in design (robustness).

In order to evaluate the second factor, we define the thermal inertia time, or time constant $\tilde{t}_c$, which is the time when the hot-spot temperature reaches the steady-state hot-spot temperature in the absence of coolant,

$$\tilde{T}_{\max,\text{no flow}}\left(\tilde{t}_c\right) = \tilde{T}_{\max,ss} \tag{27}$$

At $t = 0$, the uniform heat flux q'' lands on the left wall (Fig. 1), the tree channels are filled with stagnant coolant, and the remaining boundaries are adiabatic. The coolant temperature also rises. At $t = t_d$, the pressure difference *Be* is applied. The coolant begins to flow, and gradually changes to fully developed flow.

Fig. 6 shows numerical results of the thermal inertia time $\tilde{t}_c$ versus the pressure difference number and tree configuration (p). The effect of *Be* and p on $\tilde{t}_c$ stems from Eq. (27), in which $\tilde{T}_{\max,ss}$ depends on *Be* and p. Fig. 6 is similar to the upper part of Fig. 5. Attention must be paid to the design domain in the lower-right corner of Fig. 6. If the specified pressure difference is 3.2×10^8, the corresponding optimal structure is $p = 4$ (Fig. 3). In this case the time constant $\tilde{t}_c$ is very small, which means that if time delay is too large, the peak temperature may exceed the allowable maximum temperature and thermal integrity is damaged.

To sum up, a complex tree-shaped flow architecture is preferable when the imposed pressure difference is large. While this structure brings the benefit of a fast cooling response, it also has a short $\tilde{t}_c$. Therefore, it is required to evaluate the effect of the time delay on the transient peak temperature and determine the allowable time delay such that the peak temperature in transition does not surpass the peak temperature under steady-state conditions.

The time delay before the start of the flow of coolant is set in relation to t_c, as a fraction of the time constant determined in Eq. (27) and Fig. 6,

$$\tau = \frac{\tilde{t}_d}{\tilde{t}_c} \tag{28}$$

As shown in Fig. 7, when the relative time delay τ is larger than a critical value (called τ_*), the peak temperature overshoots the steady-state level. It is assumed that the solid material and its functions can withstand the steady-state peak temperature, but fail when the hot-spot temperature exceeds the steady-state peak temperature. The allowable peak temperature is the peak

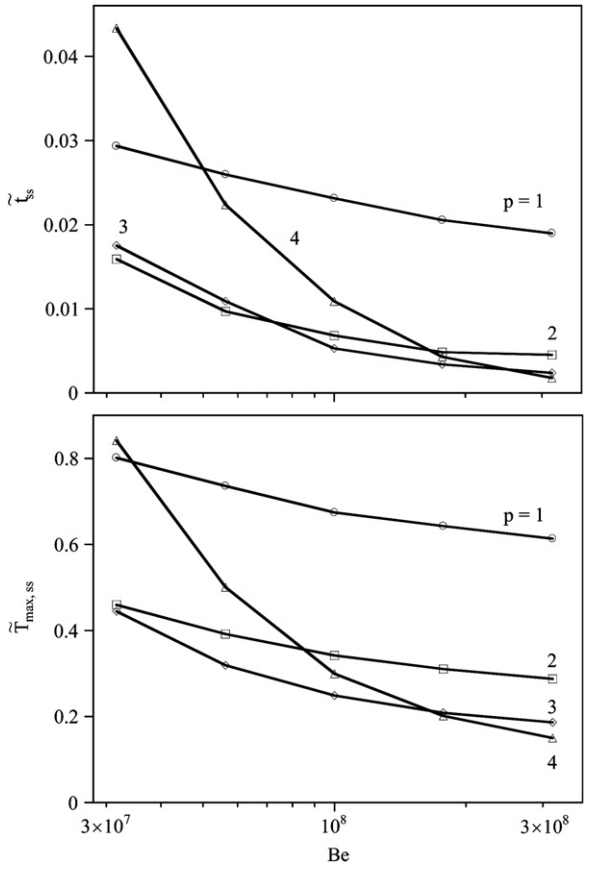

Fig. 5. The effect of *Be* and p on the characteristic time and the steady-state peak temperature.

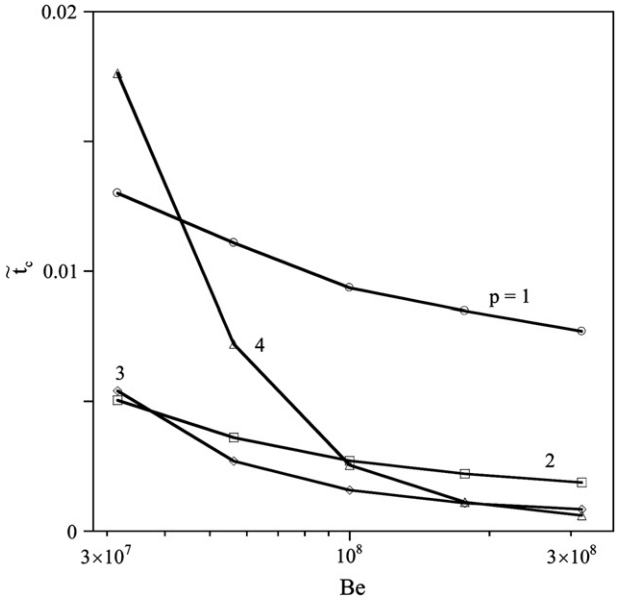

Fig. 6. The effect of *Be* and p on the thermal inertia time $\tilde{t}_c$.

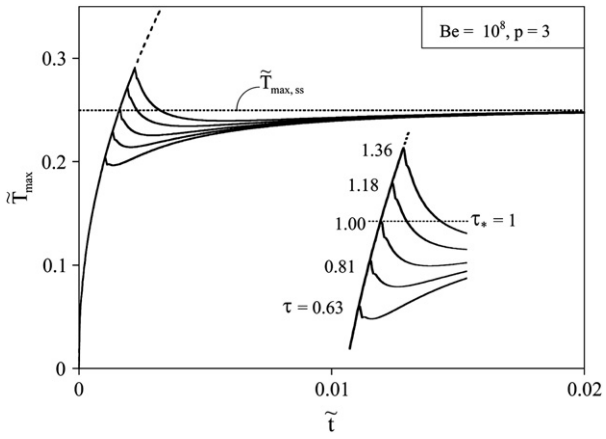

Fig. 7. The effect of the time delay τ on the peak temperature when $Be = 10^8$ and $p = 3$.

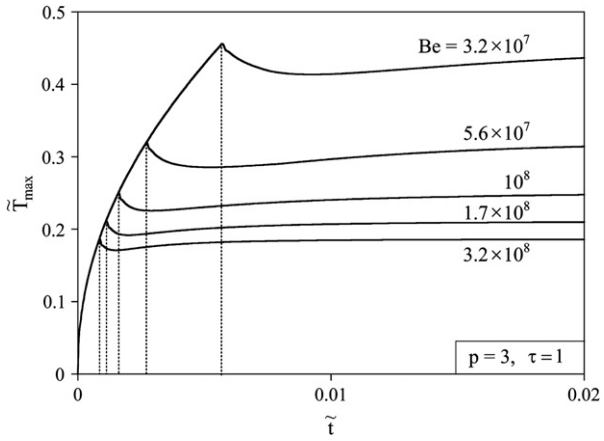

Fig. 9. The effect of the pressure difference Be on the critical delay τ_* when $p = 3$.

temperature under steady-state conditions. Therefore, the critical time delay τ_* is a measure of the longest delay time within which the vascular structure remains safe.

Fig. 7 shows the evolution of the peak temperature when a time delay exists. During the delay time there is no flow and the hot-spot temperature rises rapidly. When the coolant begins to flow, the rise of $\tilde{T}_{max}$ stops, and the trend is reversed. The horizontal dashed line shows the level of the steady-state peak temperature, or the allowable peak temperature. When the time delay τ is equal to or less than approximately 1, the transient peak temperature is kept under the allowable level. When τ is greater than 1, overheating occurs. In conclusion, for the design studied in Fig. 7 the critical delay is $\tau_* \cong 1$, and this means that in this case t_d is essentially equal to t_c.

Fig. 8 shows the temperature distribution on the heated side of the wall (the left side in Fig. 1a), on only the upper half of the surface, i.e. in the vicinity of the upper eight outlets. Immediately after the start of cooling (at $\tilde{t}_d + 6 \times 10^{-5}$), the hot spots are concentrated in two places, between the upper two outlets and between the lower two, although the upper hot spot is the hottest. A little later ($\tilde{t}_d + 1.2 \times 10^{-4}$) the hot spots jump outside the dendrite, above the upper outlet, and below the lower outlet. This time the hottest spot is the lower hot spot because of a difference in mass flow rates: the flow rate through the uppermost outlet exceeds by 7.3% the flow rate through the lowest outlet.

Next, we investigated the effect of the pressure difference Be on the critical delay τ_*. Fig. 9 shows the evolution of peak temperature for various pressure difference numbers when the delay time τ is set at 1 (i.e. $t_d = t_c$, and the coolant begins to flow at $t = t_c$) and $p = 3$. The reason why the flow of the coolant was initiated early for the simulations with high Be is that a higher pressure difference results in a shorter thermal inertia time $\tilde{t}_c$ (Fig. 6). The simulations show an infinitesimal overshoot right after the start of the coolant, which is indicated with dashed lines in Fig. 9. A larger overshoot results from a lower pressure difference. However, the overshoots are less than 0.2% of the allowable peak temperature for all the simulations. In other words, the critical delay τ_* is nearly 1. When the delay $\tilde{t}_d$ is shorter than the thermal inertia time $\tilde{t}_c$, the system is thermally safe. As a result, although a low pressure difference causes an overshoot and the allowable delay time, the effect is small enough

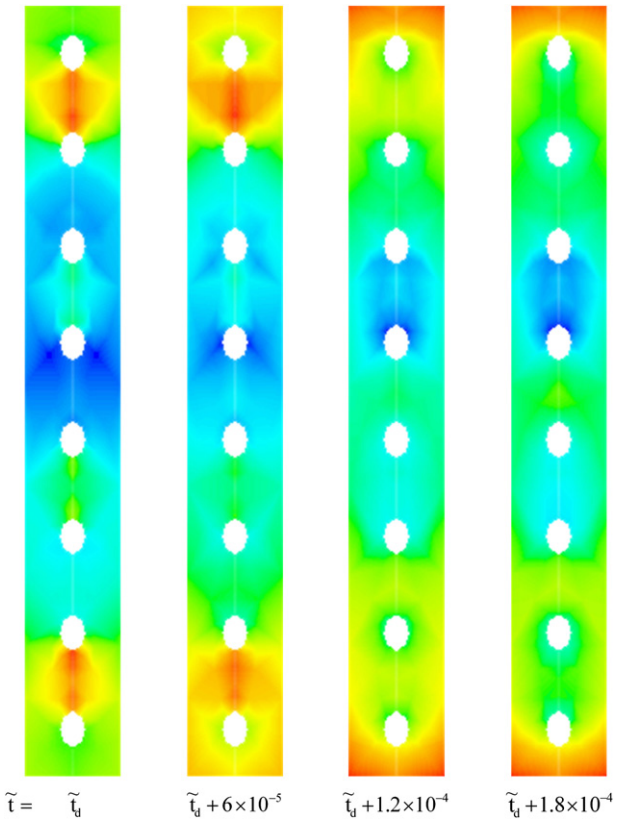

Fig. 8. The migration of the hot spots after the coolant starts flowing: the temperature distribution on the heated (left) side in Fig. 1a ($p = 3$), in the vicinity of the upper eight outlets.

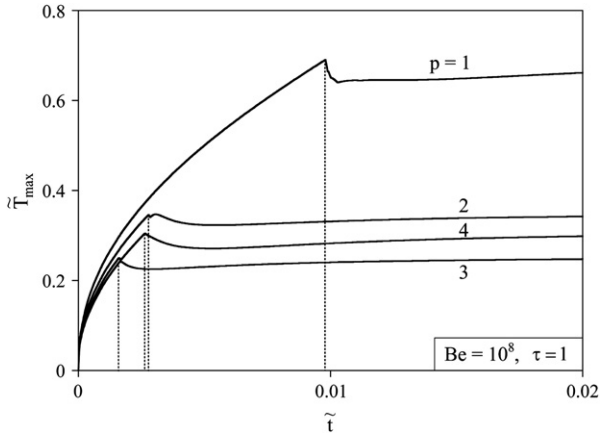

Fig. 10. The effect of the number of bifurcation levels p on the critical delay τ_* when $Be = 10^8$.

to ignore. The allowable delay time is essentially the same as the thermal inertia time $\tilde{t}_c$.

Fig. 10 shows the effect of the number of bifurcation levels (p) on the critical delay τ_* when $\tau = 1$ and $Be = 10^8$. Here we see again that there are small overshoots after the start of coolant flow, which are indicated with dashed lines in Fig. 10. This means that thermal inertia at hot spots is negligible. The simulations show that regardless of complexity of the structure the allowable delay time is equal to the thermal inertia time $\tilde{t}_c$.

5. Conclusions

To summarize, during the delay time the hot spots are located in the vicinity of the coolant outlets on the heated side, as shown on the left of Fig. 8. As soon as a pressure difference initiates the flow of coolant, the hot spots are swept away, almost instantly. This explains why the critical delay τ_* is nearly 1.

An important finding is that the complexity of the dendritic architecture has an effect on the thermal response following sudden heating and sudden cooling by fluid flow. When the driving pressure difference is fixed, the approach to the steady-state temperature is the shortest when the architecture has an optimal number of bifurcation levels (Figs. 4 and 5)

Acknowledgement

This research was supported by the Air Force Office of Scientific Research based on a Grant for "Constructal Technology for Thermal Management of Aircraft". We thank Dr. David Moorhouse (Air Force Research Laboratory) for the advice and guidance that he gives us in this research direction.

References

[1] A. Bejan, S. Lorente, Design with Constructal Theory, Wiley, Hoboken, 2008.
[2] A. Bejan, Advanced Engineering Thermodynamics, second ed. Wiley, New York, 1997.
[3] A. Bejan, Shape and Structure, from Engineering to Nature, Cambridge University Press, Cambridge, UK, 2000.
[4] A. Bejan, S. Lorente, Constructal theory of generation of configuration in nature and engineering, J. Appl. Phys. 100 (2006) 041301.
[5] A. Heitor Reis, Constructal theory: from engineering to physics, and how flow systems develop shape and structure, Appl. Mech. Rev. 59 (2006) 269–282.
[6] G. Hernandez, J.K. Allen, F. Mistree, Platform design for customizable products as a problem of access in a geometric space, Eng. Optimiz. 35 (2003) 229–254.
[7] Y. Chen, P. Cheng, An experimental investigation on the thermal efficiency of fractal tree-like microchannel nets, Int. Comm. Heat Mass Transfer 32 (2005) 931–938.
[8] S.M. Senn, D. Poulikakos, Tree network channels as fluid distributors constructing double-staircase polymer electrolyte fuel cells, J. Appl. Phys. 96 (2004) 842–852.
[9] F. Lundell, B. Thonon, J.A. Gruss, Constructal networks for efficient cooling/heating, in: Second Conference on Microchannels and Minichannels, Rochester, NY, 2004.
[10] M. Lallemand, F. Ayela, M. Favre-Marinet, A. Gruss, D. Maillet, P. Marty, H. Peerhossaini, L. Tadrist, in: Thermal Transfer in Microchannels: Applications to Micro-Exchangers, French Congress on Thermics, SFT 2005, Reims, 30 May–2 June 2005.
[11] N. Kockmann, T. Kiefer, M. Engler, P. Woias, Channel networks for optimal heat transfer and high throughput mixers, in: ECI International Conference on Heat Transfer and Fluid Flow in Microscale, Castelvecchio Pascoli, Italy, September 2005.
[12] Y.S. Muzychka, Constructal design of forced convection cooled microchannel heat sinks and heat exchangers, Int. J. Heat Mass Transfer 48 (2005) 3119–3127.
[13] Y.S. Muzychka, Constructal multi-scale design of compact micro-tube heat sinks and heat exchangers, Int. J. Therm. Sci. 46 (2007) 245–252.
[14] D.V. Pence, Reduced pumping power and wall temperature in microchannel heat sinks with fractal-like branching channel networks, Microscale Thermophys. Eng. 6 (2002) 319–330.
[15] A.Y. Alharbi, D.V. Pence, R.N. Cullion, Fluid flow through microscale fractal-like branching channel networks, J. Fluids Eng. 125 (2003) 1051–1057.
[16] S. Lorente, A. Bejan, Heterogeneous porous media as multiscale structures for maximum flow access, J. Appl. Phys. 100 (2006) 114909.
[17] S. Lorente, W. Wechsatol, A. Bejan, Tree-shaped flow structures designed by minimizing path lengths, Int. J. Heat Mass Transfer 45 (2002) 3299–3312.
[18] C.D. Murray, The physiological principle of minimal work in the vascular system, and the cost of blood-volume, Proc. Acad. Natl. Sci. 12 (1926) 207–214.
[19] W.R. Hess, Das Prinzip des kleinsten Kraftverbrauches im Dienste hämodynamischer Forschung, Arch. Anat. Physiol. (1914) 1–62.
[20] S. Lorente, A. Bejan, Svelteness, freedom to morph, and constructal multi-scale flow structures, Int. J. Therm. Sci. 44 (2005) 1123–1130.
[21] STARCCM+ (Version 1.04) basics, CD-adapco Company.
[22] S. Bhattacharjee, W.L. Grosshandler, The formation of a wall jet near a high temperature wall under microgravity environment, ASME HTD 96 (1988) 711–716.
[23] S. Petrescu, Comments on the optimal spacing of parallel plates cooled by forced convection, Int. J. Heat Mass Transfer 37 (1994) 1283.